Journal Name

Understanding the structural diversity of freestanding Al$_2$O$_3$ ultrathin films through a DFTB-aided genetic algorithm[†]

Maxime Van den Bossche,[a] Claudine Noguera,[a] and Jacek Goniakowski [a]

(Sub)nanometre-thin alumina films are frequently encountered due to the self-limited oxidation of Al and its alloys, and seem to display an even larger structural variety than bulk alumina itself. While the nature of the underlying substrate and the oxidation kinetics are known to modulate the structure of supported films, understanding the intrinsic stability of freestanding films constitutes an important first step in itself, especially when the interaction with the substrate is rather weak. Using a combined tight-binding/DFT genetic algorithm approach, we identify particularly stable $\theta(100)$-type films along with a host of novel stable thin film structures. Several of these correspond to cuts from relatively high energy bulk structures, e.g. dehydrated boehmite, pseudo-CaIrO$_3$, defective rocksalt and LuMnO$_3$, which are not commonly associated with alumina. DFT calculations allow to rationalize this stability reversal with respect to α-Al$_2$O$_3$ in terms of low surface energies compared to $\alpha(0001)$ and to identify the underlying mechanisms: breaking a low density of relatively weak Al-O bonds, filling of Al surface vacancies, and polarity-induced relaxation of the whole film. These observations provide interesting insights into existing supported ultrathin films.

1 Introduction

Ultrathin metal oxide films play an important role in various technologically important areas, ranging from corrosion protection, microelectronics[1,2], gas sensing,[3–5] and heterogeneous catalysis.[6–8] Thin Al$_2$O$_3$ films, in particular, are encountered when e.g. aluminium is exposed to air,[9,10] as gate dielectric in advanced transistors,[2] and as model supports for the study of catalytic phenomena.[11] Such films furthermore pose a challenge when galvanizing novel Al-containing high strength steels,[12,13] as the zinc coating only weakly adheres to the easily formed aluminium oxide layer at the steel surface.

A detailed understanding of the properties of such films requires knowledge of the oxide film structure, which is often challenging due to the considerable structural complexity of alumina, which is further increased at low dimensionality. Already for the bulk structure of Al$_2$O$_3$ many different polymorphs exist.[14] At lower dimensions, the same polymorphs may be encountered but with a different, size-dependent energetic ordering. The oth-

erwise metastable γ-Al$_2$O$_3$ has for example been found to be thermodynamically favoured over the α-phase in nanoparticles with surface areas larger than 100 m^2/g[15,16] while amorphization takes place beyond 370 m^2/g.[16,17] A similar stability inversion has been suggested for thin Al$_2$O$_3$ films on Al(111).[18] By contrast, annealing the initially amorphous oxide layer on the (100) surfaces of various transition metal aluminides results in θ-alumina.[19–24] The greater prominence of θ-alumina in thin films compared to nanoparticles is one outstanding puzzle which will be better understood through the present work.

Moreover, also entirely new structures may be found, without any correspondence to known bulk polymorphs. In the case of Al$_2$O$_3$, this has been most clearly illustrated in the case of oxidized NiAl(110),[25–27] and Ni$_3$Al(111)[28–30] surfaces. On both substrates, the circa 5 Å thin oxide layer consist of an Al$_2$O$_3$ interfacial layer of comparatively low density, covered by a dense and oxygen-deficient top layer.

Though understanding these tendencies may be a complex affair due to the influence of e.g. the underlying substrate and the growth kinetics, a comprehensive approach ought to include (or even start from) a view of the mechanisms which are responsible for thermodynamic stability in the absence of a support material, which is the aim of the present work. With regards to the substrate, this abstraction is most appropriate in the case of weak interaction between the Al$_2$O$_3$ layer and the underlying
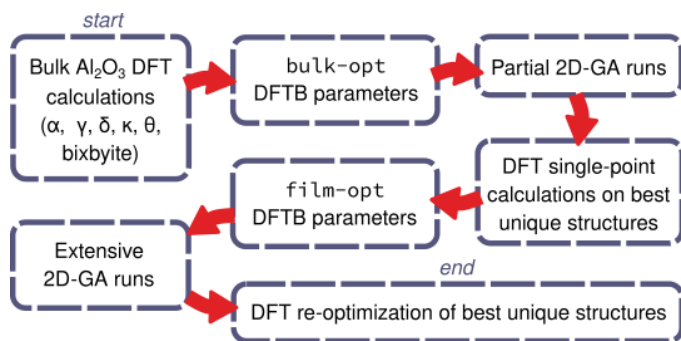
Fig. 1 Overview of the genetic algorithm for the determination of stable Al_2O_3 thin film structures, using a two-dimensional genetic algorithm (2D-GA) in conjunction with a semi-empirical electronic structure method (DFTB).

substrate. We will, however, show that several of the aforementioned supported thin films can be related to stable freestanding films, despite strong interactions with the substrate and a non-stoichiometry in the alumina layer.

To explore the structural diversity of stable (sub)nanometre Al_2O_3 layers, we have devised a genetic algorithm for thin films in combination with a semi-empirical electronic structure theory, which we will describe in the next section. The physical mechanisms favouring the ensuing configurations will then be analyzed after comparing with known low-energy surface terminations of various bulk polymorphs. Before concluding, the connection to previously characterized supported thin films will be briefly discussed.

2 Computational methods

Automatic searches of the potential energy landscape require a large number of force evaluations and hence are prohibitively expensive to carry out using non-empirical electronic structure methods such as density functional theory (DFT). Conversely, interatomic potentials demand little computing effort but are often found lacking in terms of accuracy. As a middle-of-the-road solution, we choose a density functional tight-binding (DFTB) approach with an adaptive parametrization scheme (see Figure 1). Starting from an initial parametrization optimized for bulk Al_2O_3, a limited set of genetic algorithm runs are performed in order to construct a training set for thin film structures, which allows further refinement of the DFTB parameters. A two-dimensional genetic algorithm (2D-GA) is used as the global optimization algorithm. Extensive 2D-GA searches are then carried with the film-optimized DFTB parameters, after which the most promising structures are post-processed at the DFT level. The different components of this approach will now be described in more detail.

2.1 Density functional theory

All density functional theory (DFT) calculations are performed with the VASP [31–34] implementation of Kohn-Sham DFT. [35,36] Standard projector augmented wave (PAW) setups are used to represent the core electrons with valences of 3 and 6 for Al and O, respectively. The exchange-correlation energy is described us-

ing the optB86b-vdW functional. [37,38] Brillouin-zone integration is done with Monkhorst-Pack grids [39,40] with a density of 5 k-points per $Å^{-1}$. The basis set includes plane waves with a kinetic energy up to 500 eV during geometry optimization, which is increased to 700 eV in subsequent single-point calculations to ensure convergence with respect to the basis set size. The local optimizations are pursued using the Broyden-Fletcher-Goldfarb-Shanno (BFGS) algorithm until the maximal force and stress components drop below 0.05 eV/Å and $0.01/N_{Al_2O_3}$ eV/$Å^3$, respectively. For 2D structures, only the σ_{xx}, σ_{yy}, and σ_{xy} components need to be considered. The surface energies E_{surf} of bulk-derived films are determined as

$$E_{surf} = \frac{E_{tot}^{film} - N_{f.u.}^{film} E_{tot}^{bulk}/N_{f.u.}^{bulk}}{2A}, \qquad (1)$$

with E_{tot} the total energy, $N_{f.u.}$ the number of formula units and A the surface area. We choose to calculate the formation energies E_{form} with respect to bulk α-alumina in an analogous way, i.e.

$$E_{form} = \frac{E_{tot}^{film} - N_{f.u.}^{film} E_{tot}^{\alpha}/N_{f.u.}^{\alpha}}{2A}. \qquad (2)$$

2.2 Density functional tight-binding

Self-consistent charge (SCC) DFTB represents a semi-empirical approximation to DFT, where a speedup of 2-3 orders of magnitude is gained by virtue of a minimal basis set of atomiclike orbitals, neglect of three-center integrals, a monopole expansion of interatomic charge transfer, and treatment of remaining total energy contributions via short-ranged pairwise potentials. For a detailed description of the method, the Reader is referred to the works of Frauenheim, Seifert, and coworkers (e.g. Ref. 41). The minimal basis consists of the s and p valence states of Al and O.

The main empirical ingredients are (*i*) the polynomial- or spline-based repulsive potentials V_{rep} for every element pair, and (*ii*) the harmonic potentials V_{conf} used to confine the atomic orbitals and densities from which the Hamiltonian and overlap integrals are determined. These parameters are optimized with respect to DFT total energies and forces using the `Tango` and `Hotcent` codes, [42,43] similar to the work in Ref. 44. The required atomic DFT calculations (in `GPAW` [45,46]), as well as the computation of the effective potential in the density superposition scheme, are carried out using the optB86b functional (i.e. without long-range vdW correlation) via integration with `LibXC`. [47] All actual DFTB calculations are executed with the 18.2 version of the `DFTB+` program. [48]

2.3 Genetic algorithm

The task of global structure optimization of a given compound consists of finding the most stable local minima on the potential energy landscape. As complete enumeration is computationally intractable in this high-dimensional space, [49] more efficient approaches have been developed such as simulated annealing, basin hopping, and genetic algorithms. [50,51] The present searches are performed using the genetic algorithm (GA) framework [52,53] included in the Atomic Simulation Environment (`ASE`). [54,55]

Considering that an objective function based on just the total energy will necessarily converge to very thick films, the thickness range of interest (from 3.5 to 11 Å) is divided into intervals of 1.5 Å, and a series of GA searches is performed within each interval. The thickness L_z is here defined as the difference of extremal z-coordinates in the structure. To locate the most energetically stable thin film structures with $N_{f.u.}$ formula units (i.e. $(Al_2O_3)_{N_{f.u.}}$) within a given thickness interval, the present 2D-GA assumes the following strategy:

1. Initialization of $2N_{f.u.}$ starting candidates by assigning random atomic positions within the specified interval. The **a** and **b** lattice vectors are also chosen randomly, with the constraint that $\widehat{ab}$ lies between $20°$ and $160°$ and that the resulting density corresponds to circa 1 atom per 10 Å^3.

2. The initial population is created by locally optimizing each initial structure at the DFTB level. Both the atomic forces and the stress components in the xy plane are minimized.

3. In each of the subsequent $2N_{f.u.}^2$ GA iterations, one or two structures are randomly selected (following the procedure in Ref. 53) and subjected to a randomly chosen genetic operator (listed in Table 1 in the ESI†) to create a new structure which is then also locally optimized. The population is updated so as to always contain the $2N_{f.u.}$ most stable unique structures with L_z within the chosen interval. Structural uniqueness is determined via fingerprint functions.[56]

Each search is furthermore duplicated 20 times using different random seeds. This setup allows a high (>90%) convergence rate for each of the different number of formula units employed ($N_{f.u.}$ = 4, 6 and 8 for each interval, in addition to 2 for the thinnest interval). From each series of 2D-GA runs, the 100 best unique structures at the DFTB level are extracted and subjected to DFT single-point calculations. In case the 2D-GA searches are performed with the refined `film-opt` parameter set, the 30 most stable structures after this initial screening are then re-optimized at the DFT level.

3 Results

3.1 Bulk alumina

To highlight the known structural variety of alumina, and as a basis for our subsequent calculations, we start by introducing the various known bulk Al_2O_3 polymorphs. We have considered the five most common ones (α, θ, κ, γ and δ), whose energy differences per formula unit are reported in Table 1. While the structures of the first three phases have been unambiguously resolved already early on, the γ- and δ-aluminas are less straightforward. Several models have been proposed in the literature, displaying variations in the cation vacancy positions (γ_{MG},[57] γ_{PN},[58] and δ_{RH}[59]) and/or including cations in non-spinel positions (γ_{PR},[60,61] γ_{KR},[62] δ_{KB1} and δ_{KB2}[63]).

Overall, the DFT energy differences compare favourably with the calorimetry data from Ref. 64, from which we have substracted the vibrational contributions calculated in Ref. 65. The energetical ordering, for example, is well reproduced, at least

Table 1 Relative energies (per formula unit) for various bulk Al_2O_3 polymorphs. [a] Experimental values are derived from the microcalorimetry data from Ref. 64 with substraction of the vibrational contributions calculated in Ref. 65. [b] Structures marked with * are included in the DFTB training set. The `bulk-opt` and `film-opt` labels denote the bulk- and thin film- optimized parameter sets, respectively (see text)

			ΔE (eV/f.u.)		
	Expt.[a]	Model	optB86b -vdW	DFTB[b] `bulk-opt`	DFTB[b] `film-opt`
α	0		0	0*	0
θ	–		0.15	0.08*	0.05
κ	0.12		0.15	0.11*	0.05
γ	0.31	γ_{MG}[57]	0.30	0.18*	0.22
		γ_{PN}[58]	0.30	0.19	0.22
		γ_{PR}[60,61]	0.42	0.32	0.40
		γ_{KR}[62]	0.23	0.17	0.29
δ	0.08	δ_{RH}[59]	0.43	0.34*	0.31
		δ_{KB1}[63]	0.14	0.13	0.12
		δ_{KB2}[63]	0.14	0.14	0.12
bixbyite	–		0.17	0.13*	-0.17

when the recently proposed models from Kovarik et al.[63] are considered for δ-Al_2O_3. Among the γ-alumina models, the structure with non-spinel Al^{3+} positions from Krokidis et al.[62] is found to be energetically favoured. It should furthermore be noted that the bixbyite structure is calculated to have a similar stability as the θ, κ and δ phases, though this phase has not yet been experimentally observed.

We remark that it appears very difficult, if at all possible, to accurately relate the observed energetical ordering to differences in local bonding patterns of the Al_2O_3 polymorphs, such as the type and interconnection of different polyhedra. Such an analysis is complicated by the importance of long-ranged electrostatic interactions in ionic materials such as Al_2O_3. We refer the Reader to the ESI† for further discussion on this topic.

The corresponding results with DFTB are shown in the last two columns of Table 1. The `bulk-opt` parameter set has been derived on the basis of optB86b-vdW relative energies and atomic forces pertaining to a few selected structural models (values marked with *). The training database comprises the equilibrium structures, which have furthermore been subjected to random atomic displacements (Gaussian distributed with 0.1 Å standard deviation) as well as volumetric expansion and compression (up to ±4% strain). Considering the approximative nature of DFTB as well as the comparatively small energy differences, the model performs quite acceptably. Note that the DFTB results are also calculated self-consistently, i.e. with geometry re-optimization. We also note in passing that the previously published `matsci` parameter set[67] has not been constructed with Al_2O_3 polymorphism in mind, and is hence found to perform rather poorly (see Table 2 in the ESI†).

For the second DFTB parameter set (`film-opt`), the training set is built from DFT single-point calculations on 100 thin film structures obtained via the 2D-GA with the `bulk-opt` DFTB parameters in two thickness intervals (3.5-5 Å and 6.5-8 Å, with $N_{f.u.}$ = 2 and 4, respectively). As shown by the parity diagrams in Figures 2 and 3 in the ESI†, the reparametrization indeed yields a model that is significantly more accurate for thin films. As a nec-
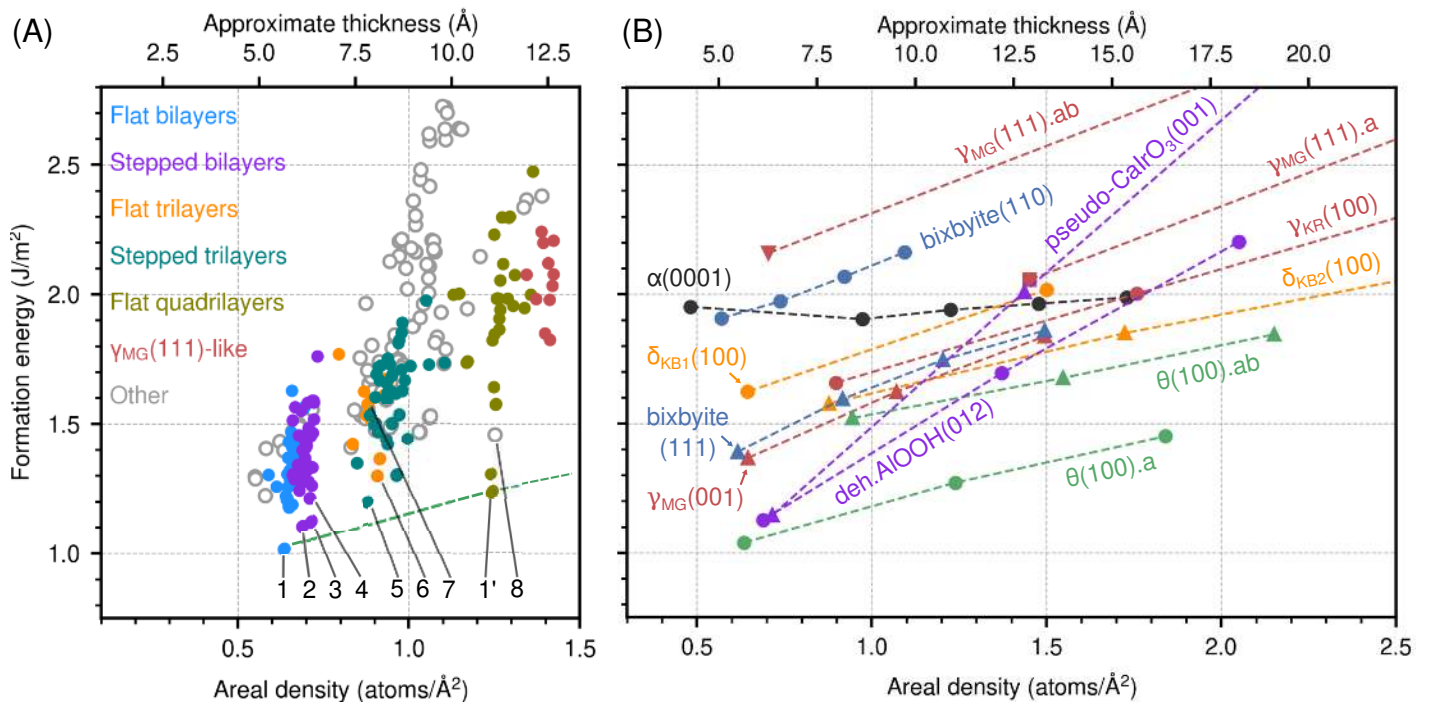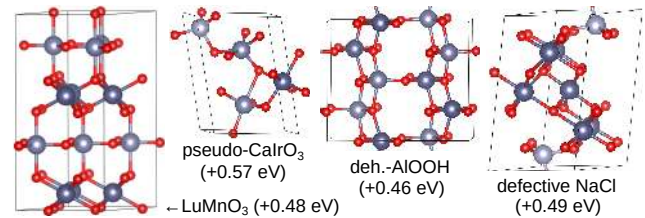
Fig. 2 Calculated formation energies with respect to bulk α-Al$_2$O$_3$ for the thin films obtained with the 2D-GA (panel A) and by cutting various bulk polymorphs (panel B). Lines are added to guide the eye.
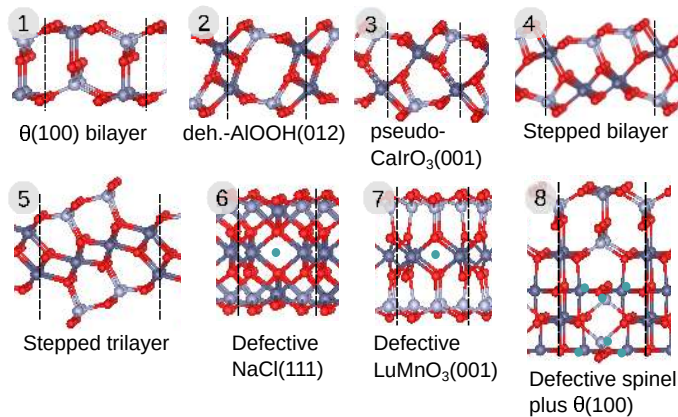
Fig. 3 Atomic models of selected films obtained via the 2D-GA. Aluminium and oxygen atoms are coloured in blue-gray and red, respectively, with cation vacancies indicated in light blue. Higher-coordinated Al atoms are given a darker shade to distinguish between 4-, 5- and 6-fold coordination. All structures in this work have been rendered with VESTA.[66]

Fig. 4 Structural models and calculated formation energies of the new bulk polymorphs, in eV per formula unit relative to α-Al$_2$O$_3$ (optB86b-vdW). Colouring as in Figure 3.

essary compromise, the energetic ordering in the bulk is less accurately described (see Table 1), where the bixbyite phase in particular is overly stabilized. For bulk-like materials, the `bulk-opt` model hence remains more appropriate. The need for separate DFTB parameter sets to optimally reproduce the DFT geometries and energetics in ultra-thin films is understandable, considering the different local environments at the surface compared to the bulk.

3.2 Thin films from 2D-GA

From the 2D-GA searches between 3.5 and 11 Å, a considerable variety of stable thin film structures are found, of which the relative stability is shown in panel A of Figure 2. As a measure of thickness, we employ here the number of atoms per surface area, which in an experimental context is better defined than the height L_z. The approximate correspondence to the latter is shown on the top horizontal axis. We will furthermore discriminate between 'bilayers', 'trilayers', and so forth, based on the number of cation planes stacked along the z direction.

Selected structures are shown in Figure 3 to illustrate the different types of geometries found. The thinnest films (L_z between 3.5 and 5 Å) correspond to relatively flat O-Al/O/Al-O bilayer structures (blue dots), of which the most stable configuration is a $\theta(100)$ bilayer (#**1**). Other structures within this class typically feature outer Al-O layers with a higher degree of hexagonal order (i.e. containing (AlO)$_3$ hexagons).

At slightly larger thicknesses, the main types are bilayers with step-like corrugations (purple dots), with structures #**2**, #**3** and
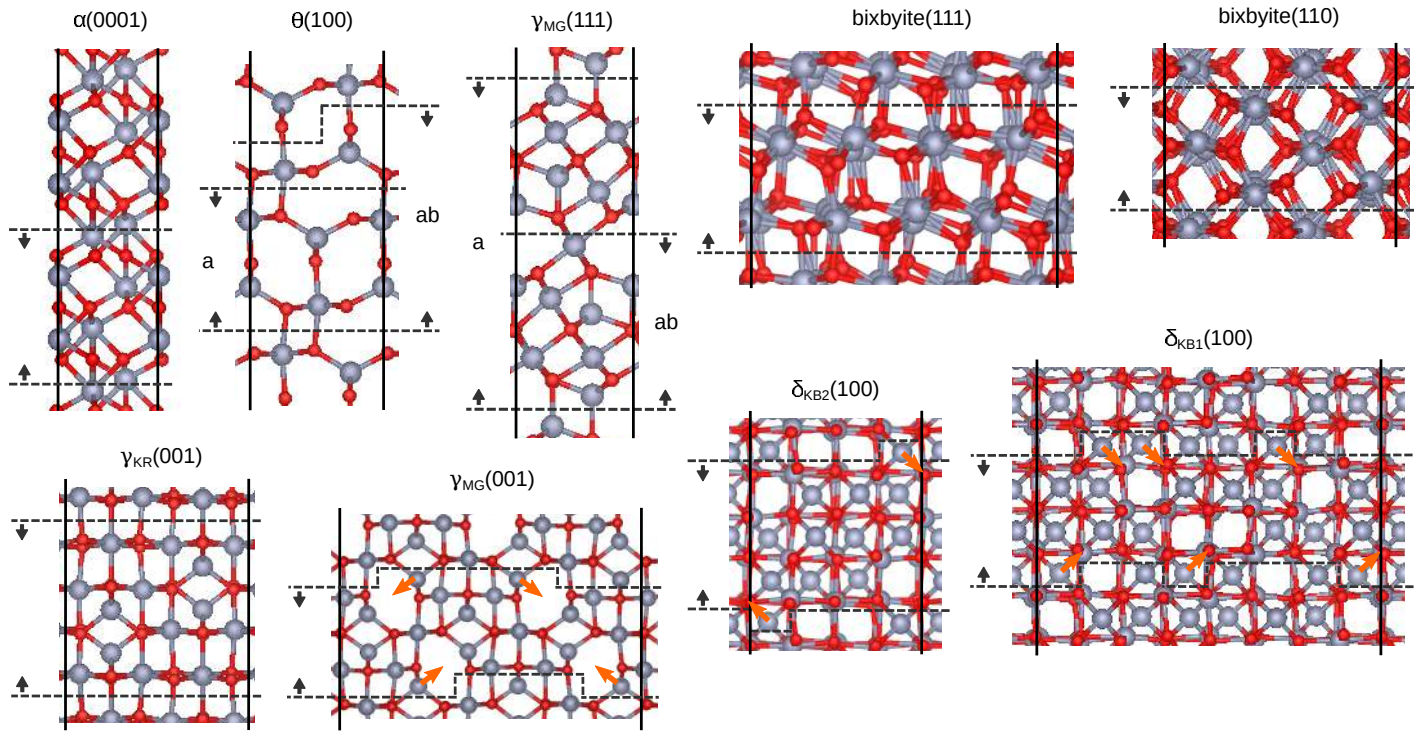
Fig. 5 Atomic structures of the bulk-derived thin films. The labelling and colouring are as in Figure 2 and 3, respectively. Horizontal lines indicate the boundaries of the thinnest film in each series. Displacements of surface Al atoms into nearby vacancies are indicated with orange arrows.

#**4** as the most energetically favourable arrangements. We identify #**2** as derived from fully dehydrated boehmite (denoted as deh.-AlOOH) and with stoichiometry Al_2O_3. A similar structure has been proposed as a hypothetical intermediate in the conversion of boehmite (γ-AlOOH) to γ-Al_2O_3.[62] The bulk structure of #**3** resembles the high-pressure $CaIrO_3$ alumina phase[68,69] and will be referred to as *pseudo*-$CaIrO_3$. The stability of such films is quite remarkable, considering the large energy of the two respective bulk phases (see Figure 4).

In the 0.8 to 1.1 atoms/Å^2 interval (ca. 7 to 9 Å), O_3-Al_3/O_3-Al_2-O_3/Al_3-O_3-ordered trilayer structures are obtained, both with comparatively flat and stepped surface layers (orange and teal dots, respectively). #**6** is the most stable arrangement in the first category and represents a defective, anion-terminated rocksalt(111) film. An interesting variant, #**7**, can be regarded as a defective $LuMnO_3$(001)-type film. The corresponding bulk structures are also shown in Figure 4. In both cases, the outer layers consist entirely of $(AlO)_3$ hexagons, with the inner Al atoms being similarly arranged but with one third octahedral vacancies. Many stepped variants exist, with structure #**5** possessing the lowest formation energy.

At the highest investigated thicknesses, mainly quadrilayers and γ_{MG}(111)-like films are found (green and red dots). The most stable quadrilayer structure (#**1'**) represents a θ(100) cuts as in structure #**1**, but at double thickness. At slightly higher energies one finds other θ(100)-like films with stacking faults. Structure (#**8**) consists of a superposition of θ(100) and defective spinel(100) layers.

3.3 Thin films from bulk cuts

In order to explain the calculated relative film stabilities, different approaches can be envisaged. One may for example attempt to interpret the relative energy differences directly in terms of differences in local bonding patterns. The difficulties of such an analysis for the present material have however already been emphasized in Section 3.1. We have opted for a different approach where the relative bulk stabilities are taken as a starting point and where the focus lies on the energy required to create thin films from the bulk. To this end, we have found it useful to compare with a series of thin films constructed from low-energy terminations of the bulk polymorphs (structures shown in Figure 5):

- the Al-terminated (0001) surface for α-Al_2O_3,[70–72]
- the (100) orientation for θ-Al_2O_3,[73,74]
- the (001) and (111) surfaces for the γ_{MG} defective spinel,[58]
- the (001) surface for γ_{KR}-Al_2O_3,[75]
- the (100) surface of the δ_{KB1} and δ_{KB2} models, having a similar surface structure as the spinel-type γ(001) slabs,
- the (111) and (110) bixbyite surfaces, which have been identified as the lowest-energy terminations for bixbyite In_2O_3,[76]
- the (012) and (001) of the newly found dehydrated boehmite and pseudo-$CaIrO_3$ phases, respectively.

For θ(100) and γ_{MG}(111), two different film types are considered: '*a*' cuts where the most stable termination is exposed on both sides and '*ab*' cuts where the next-most-stable termination is used on one of the two sides.

The thickness-dependent formation energies with respect to α-Al$_2$O$_3$ are shown in panel B of Figure 2. In agreement with the 2D-GA results, $\theta(100)$.a films are found to be the most stable at their respective thicknesses (green circles). In the 5 to 15 Å range, a sizeable gap exists until the next-most stable thin films cut from known bulk polymorphs, such as $\gamma_{MG}(001)$, $\theta(100)$.ab, bixbyite(111) and $\delta_{KB2}(100)$. The 2D-GA searches, however, demonstrate that many new structures can be found in this region, such as those corresponding to dehydrated boehmite and pseudo-CaIrO$_3$ (purple dots and triangles, respectively).

4 Discussion

We now possess sufficient data to analyze the peculiar polymorphism of Al$_2$O$_3$ at low thicknesses. First, we will formulate an explanation for the underlying physical mechanisms that are at play in the freestanding thin films. This is followed by a brief discussion to highlight the connections of our results to experimental observations of supported alumina thin films.

4.1 Polymorphism in freestanding films

Our starting point for understanding the stability trends in Figure 2 is that, for sufficiently thick films, the formation energies given by Eq. 2 can be rewritten as follows:

$$E_{\text{form}} = E_{\text{surf}} + \Delta E_{\text{bulk}} \left(\frac{N_{f.u.}^{film}}{2A} \right), \qquad (3)$$

with ΔE_{bulk} the energy per formula unit of the parent bulk phase with respect to α-Al$_2$O$_3$. In this regime, the (linear) thickness dependence of the formation energies is simply due to the difference in bulk energies. At low thickness, certain deviations are to be expected, due to e.g. relaxation in the xy plane and finite-size electronic effects. However, we find that such deviations are comparatively small here, except for pseudo-CaIrO$_3$(001) which will be discussed separately. In Figure 2(B), we indeed retrieve a near-zero slope for $\alpha(0001)$ and increasingly steep slopes with increasing relative bulk energies for the other polymorphs (see also Table 1 and Figure 4).

For the thinnest films, between 5 to 10 Å thick, however, the surface energy term is visibly more important than the difference in bulk energies. To further analyze this aspect, we show the surface energies E_{surf} in Figure 6 (top panel, green bars), calculated for the thickest investigated films and ordered by increasing formation energy at circa 0.6 atoms per Å^2. We indeed find that the relative ordering mainly follows the computed E_{surf}, though the influence of ΔE_{bulk} is certainly non-negligible for cases such as the pseudo-CaIrO$_3$(001)(thin) and deh.-AlOOH(012). It is furthermore instructive to consider the surface energies before ionic relaxation (blue bars). For most surfaces, the contributions from ionic relaxation are of a similar magnitude and do not alter the relative ordering. In certain cases, however, this contribution is noticeably larger (marked with stars), which will be further analyzed in paragraph 4.1.2.
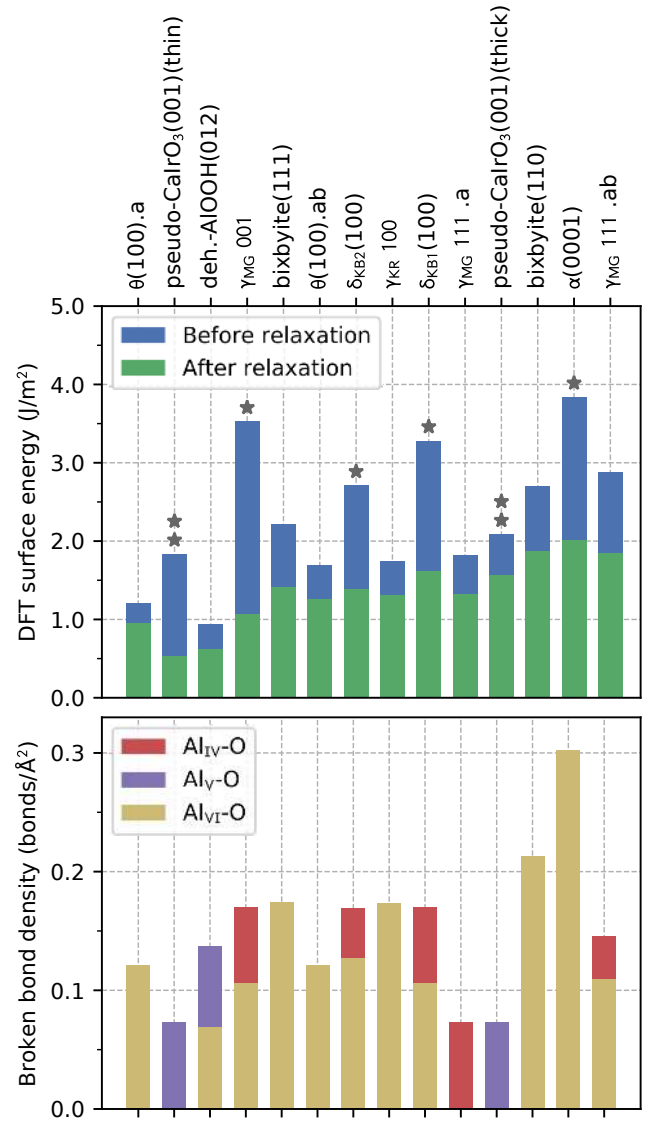

Fig. 6 Top: calculated surface energies before and after ionic relaxation. Surfaces with pronounced stabilization upon relaxation and with thickness-dependent surface energies are marked with single and double stars, respectively. Bottom: densities of different bond types in the cutting plane.

4.1.1 Effects of bond breaking.

Interpreting trends in (unrelaxed) surface energies has frequently been done in terms of Al-O bonds being broken at the surface, both for metals[77] and oxides.[78] In this picture, higher surface energies result from breaking stronger bonds and/or a higher density of bonds. The bottom panel in Figure 6 shows the densities and types of broken bonds. Focusing first on the cases involving only 6-fold coordinated Al, we note that the unrelaxed surface energies indeed scale with the density of Al$_{VI}$-O bonds being cut. The low surface energy of the $\theta(100)$.a surface (in line with previous reports[73,74]) is therefore connected to the low density of these bonds in the cutting plane.

The surface energies of unrelaxed $\gamma_{MG}(111)$.a, $\gamma_{MG}(111)$.ab, $\gamma_{MG}(001)$, $\delta_{KB1}(100)$ and $\delta_{KB2}(100)$ can also be accounted for, when taking the average Al$_{IV}$-O bond strength larger than that
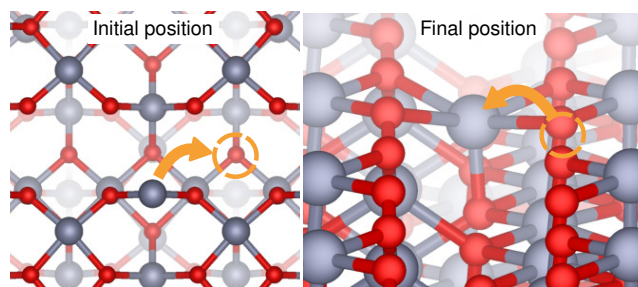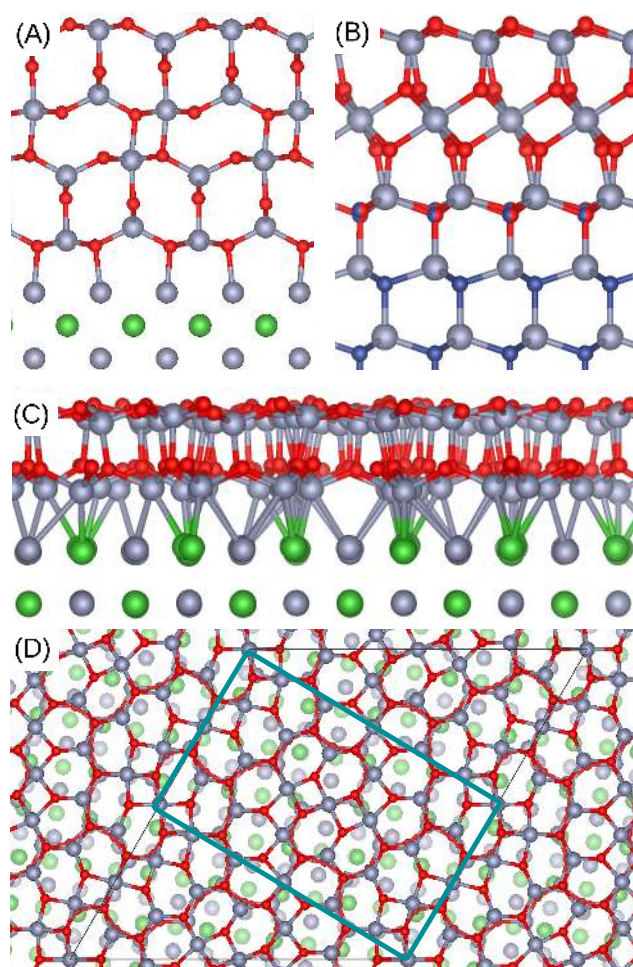
Fig. 7 Top and side views of a cation vacancy being refilled by an Al adatom on the $\gamma_{MG}(001)$ surface.
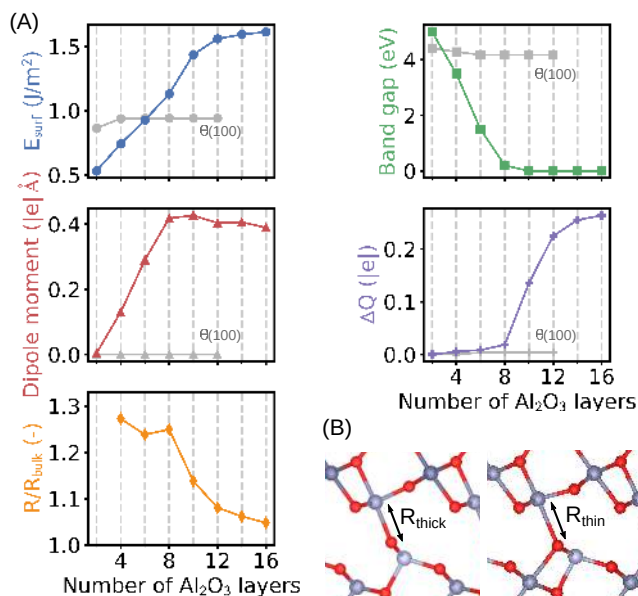
Fig. 8 Panel A: thickness-dependent properties of pseudo-CaIrO$_3$(001) films. The charge transfer ΔQ is calculated as the sum of Bader charge deviations (with respect to the bulk) of two outer bilayers. For comparison, the corresponding properties of $\theta(100)$.a films are shown in gray. Panel B: models showing the different structure inside a 'thick', bulk-like 12-layer film (top) and a 'thin' 6-layer film (bottom).

Fig. 9 Atomic structures of supported thin films (colour coding as in Figure 5 and with Ni and N in green and dark blue, respectively). (A): 1 nm thick $\theta(100)$ film on NiAl(100); (B): the native surface oxide on wurtzite-AlN(0001) (see Ref. 81); (C) and (D): the 5 Å thin Al$_{80}$O$_{104}$ film on NiAl(110) (see Ref. 27).

of Al$_{VI}$-O (roughly twice). This is in line with the general trend of increasing bond strengths and decreasing bond lengths with decreasing coordination numbers. [79,80]

The low surface energy of the unrelaxed deh.-AlOOH(012) surface, however, suggests that Al$_V$-O bonds are weaker than Al$_{VI}$-O ones. Though this does not follow the expected correlation, it remains consistent with the comparatively high energy of the bulk phases containing five-fold coordinated Al (see Figure 4). If the lower stability of this local environment appears in contradiction with the surface energies of the unrelaxed pseudo-CaIrO$_3$(001) films, we will show in the next paragraph that these films are destabilized due to effects of polarity. Lastly, we note that creating the (001) surface of LuMnO$_3$-type Al$_2$O$_3$ involves breaking a similar density of weak Al$_V$-O as for deh.-AlOOH(012). A further analysis of the corresponding trilayer structure #**7** is, however, complicated by the presence of a cation vacancy in the middle.

4.1.2 Effects of relaxation.

While the broken bond picture succeeds in explaining the surface energy before ionic relaxation, additional mechanisms need to be considered when the effect of relaxation is large (single stars in Figure 6) and strongly thickness-dependent (double stars). The $\alpha(0001)$ surface, to start, presents an ordinary situation characterized by a considerable inward relaxation of an Al surface atom with low (3-fold) coordination. [82–84] Despite this stabilization, the surface energy of $\alpha(0001)$ after relaxation remains the highest of the different bulk terminations investigated here. More profound effects on the relative stabilities are found to occur via two other mechanisms.

The first mechanism takes place on the $\gamma_{MG}(001)$, $\delta_{KB1}(100)$ and $\delta_{KB2}(100)$ surfaces, where substantial energy gains are associated with the filling of surface cation vacancies by Al surface atoms with low initial coordination. The directions of these displacements are indicated in Figure 5, while a more detailed view is given in Figure 7 for $\gamma_{MG}(001)$. Additional figures for $\delta_{KB1}(100)$ and $\delta_{KB2}(100)$ are presented in the ESI†. On all three

surfaces, the Al atom coordination increases from two-fold to five-fold, resulting in an energy gain per filled vacancy that is relatively constant across the different surfaces (circa 7 eV). The same stabilization mechanism is also expected to operate in the case of defective rocksalt(111) films, where a vacancy is filled by a three-fold coordinated Al surface atom.

Secondly, a thickness-dependent relaxation effect occurs in pseudo-CaIrO$_3$(001), where a strong contribution is found in the thin films (5 Å), but not in thicker films. The absence of centrosymmetry in the unrelaxed structures suggests the influence of polarity.[85] To confirm this interpretation, the thickness dependence of the surface energy and several other properties are displayed in Panel A of Figure 8. For comparison, the same properties are also shown for non-polar $\theta(100)$.a films (gray color) where the thickness dependence is very limited. For pseudo-CaIrO$_3$(001) films below a critical thickness of 8-10 Al$_2$O$_3$ layers, the surface polarity is uncompensated and the film dipole (red line) grows with increasing thickness. This buildup is partially attenuated by atomic displacements throughout the whole film, in contrast with the vacancy refilling mechanism where only the surface is affected. The transformation inside the film is shown in Panel B of figure 8, with indication of one Al-O bond which elongates considerably in thinner films (R/R$_{bulk}$, gold lines). At large thicknesses, the film dipole is sufficiently large to close the band gap (green line), resulting in a charge transfer between atoms on opposite sides of the film (purple line). These phenomena are similar to what has been previously described in polar MgO thin films with a zincblende(111) structure.[86] As a result, the surface energy in the ultra-thin regime increases approximately linearly with the film thickness and hence contributes to the corresponding increase in the formation energy with respect to α-Al$_2$O$_3$ shown in Figure 2. For comparison, we find this contribution to be approximately equivalent to a ΔE_{bulk} value of 0.05 eV per formula unit.

4.1.3 Mechanisms of film stabilization.

With these insights, we may now draw a full picture of the different mechanisms responsible for the relative thin film stabilities, in particular the question why the energetic ordering is so different from the bulk, leading to the appearance of entirely new structures. Our analysis points to the increased importance of the surface energy at low thickness, allowing thin films derived from higher-energy bulk phases to become energetically favourable if the associated surface energies are sufficiently low. The relative instability of the $\alpha(0001)$-type films (mainly due to the high density of broken Al$_{VI}$-O bonds) thus allows a variety of other structures to compete at low thickness (i.e. below ca. 3 nm). This influence of the surface energy is already known from previous studies on low-dimensional oxides.[87,88]

A more original result is that several of these thin films originate from new bulk phases which are much less stable than the well-known transition aluminas. Particularly low surface energies are required for stabilizing such structures. We find three mechanisms to be influential in generating low surface energies:

(i) Breaking fewer and/or weaker bonds, exemplified by e.g. the $\theta(100)$.a, $\theta(100)$.ab and deh.-AlOOH(012) surfaces. The existence of the LuMnO$_3$ trilayer structure can also be viewed in this light.

(ii) Refilling of surface vacancies by terminal Al atoms, yielding considerable stabilization in the case of $\gamma_{MG}(001)$ and the defective rocksalt(111) trilayer.

(iii) Polarity-induced whole-film relaxation: similarly, strong relaxation effects may stabilize non-compensated polar terminations in sufficiently thin films, as in the case of pseudo-CaIrO$_3$(001).

It is furthermore worth noting that surface energies also play a decisive role in the polymorphism of Al$_2$O$_3$ *nanoparticles*, where amorphous and γ-type structures are favoured over the α-phase at high specific surface areas.[15–17] The presence of various orientations, however, implies that bulk phases which yield very stable two-dimensional films (such as θ-alumina) are not necessarily also energetically preferred in nanoparticles.

4.2 Connections to supported thin films

We will now briefly discuss several results of the literature on supported thin films, showing the relevance of the above results. Firstly, the intrinsic stability of $\theta(100)$-type films is likely to lie at the origin of the experimental observation of such structures on the Al-terminated (100) surfaces of NiAl,[19–21] CoAl[22] and FeAl[23,24] (see panel A of Figure 9). We indeed find that the adhesion of a $\theta(100)$ film is comparatively weak on these substrates, amounting to circa 1.0 J/m^2 with the present computational setup. This suggests that the preference for a $\theta(100)$-type film proceeds mainly from the inherent stability of the corresponding freestanding structure.

Also structures #**6** and #**7** can be connected to two types of experimentally observed supported thin films. The first is exemplified by the native ultrathin oxide on wurtzite AlN(0001)[81] (shown in panel B of Figure 9), with similar arrangements also encountered in inversion domain boundaries in other wurtzite structures.[89–94] The second kind comprises the 5 Å thick, non-stoichiometric oxide layer on NiAl(110). First thought to resemble $\alpha(0001)$ or $\gamma(111)$[25] and even $\kappa(00\bar{1})$,[26] it has then been conclusively shown[27] to be distinct from any common alumina polymorph (model displayed in panels C and D). A similar structure has also been observed on Ni$_3$Al(111).[28–30] Through comparison with structure #**7**, however, one can show that these films are structurally related to a stoichiometric alumina thin film, which is in turn derived from a LuMnO$_3$-like bulk compound. Starting from the upper Al$_2$-O$_3$/Al$_3$-O$_3$ layers in #**7**, the surface oxides can namely be constructed by additionally introducing (*i*) inversion domain boundaries in the hexagonal AlO top layer and (*ii*) pentagon-heptagon defects in the interfacial Al$_2$O$_3$ layer.

5 Conclusions

We have explored the structural diversity of freestanding alumina thin films derived from known bulk polytypes as well as from a DFTB-aided genetic algorithm. Optimized DFTB parameter sets are furthermore provided for the simulation of Al$_2$O$_3$ (nano)materials. Our results clearly demonstrate how crystal structures other than corundum become energetically favoured

when the film is sufficiently thin (below at least 3 nm). At certain thicknesses, cuts from known bulk Al_2O_3 polymorphs are found to be globally stable (i.e. $\theta(100)$ at circa 5 and 10 Å), while at other thicknesses unexpected novel configurations are found, such as dehydrated boehmite- and pseudo-$CaIrO_3$-type structures at circa 6 Å and defective NaCl and $LuMnO_3$ at circa 7-8 Å. We show that the low surface energies required to stabilize metastable bulk phases in thin films are made possible through *(i)* the breaking of few and/or weak Al-O bonds, *(ii)* surface cation vacancy refilling, and/or *(iii)* polarity-induced whole-film relaxation. These findings are furthermore shown to be directly linked to the study of supported alumina films, with Al oxides on AlN and NiAl given as examples.

Conflicts of interest

There are no conflicts to declare.

Acknowledgements

Notes and references

1 J. S. Park, W.-J. Maeng, H.-S. Kim and J.-S. Park, *Thin Solid Films*, 2012, **520**, 1679–1693.

2 E. Fortunato, P. Barquinha and R. Martins, *Adv. Mater.*, 2012, **24**, 2945–2986.

3 Y.-F. Sun, S.-B. Liu, F.-L. Meng, J.-Y. Liu, Z. Jin, L.-T. Kong and J.-H. Liu, *Sensors*, 2012, **12**, 2610–2631.

4 K. T. Butler and A. Walsh, *Thin Solid Films*, 2014, **559**, 64–68.

5 A. Dey, *Mater. Sci. Eng., B*, 2018, **229**, 206–217.

6 M. S. Chen and D. W. Goodman, *J. Phys.: Condens. Matter*, 2008, **20**, 264013.

7 J. Gustafson, R. Westerström, O. Balmes, A. Resta, R. van Rijn, X. Torrelles, C. T. Herbschleb, J. W. M. Frenken and E. Lundgren, *J. Phys. Chem. C*, 2010, **114**, 4580–4583.

8 S. Shaikhutdinov and H.-J. Freund, *Annu. Rev. Phys. Chem.*, 2012, **63**, 619–633.

9 N. Cabrera and N. F. Mott, *Rep. Prog. Phys.*, 1949, **12**, 163.

10 J. D. Baran, H. Grönbeck and A. Hellman, *Phys. Rev. Lett.*, 2014, **112**, 146103.

11 H.-J. Freund, *Surf. Sci.*, 2007, **601**, 1438–1442.

12 P. Drillet, Z. Zermout, D. Bouleau, J. Mataigne and S. Claessens, *Rev. Met. Paris*, 2004, **101**, 831–837.

13 H.-L. T. Le, J. Goniakowski, C. Noguera, A. Koltsov and J.-M. Mataigne, *J. Phys. Chem. C*, 2016, **120**, 9836–9844.

14 I. Levin and D. Brandon, *J. Am. Ceram. Soc.*, 1998, **81**, 1995–2012.

15 J. M. McHale, A. Auroux, A. J. Perrotta and A. Navrotsky, *Science*, 1997, **277**, 788–791.

16 G. Laurens, D. Amans, J. Lam and A.-R. Allouche, *Phys. Rev. B*, 2020, **101**, 045427.

17 A. H. Tavakoli, P. S. Maram, S. J. Widgeon, J. Rufner, K. van Benthem, S. Ushakov, S. Sen and A. Navrotsky, *J. Phys. Chem. C*, 2013, **117**, 17123–17130.

18 M. Aykol and K. A. Persson, *ACS Appl. Mater. Interfaces*, 2018, **10**, 3039–3045.

19 P. Gassmann, R. Franchy and H. Ibach, *Surf. Sci.*, 1994, **319**, 95–109.

20 R.-P. Blum, D. Ahlbehrendt and H. Niehus, *Surf. Sci.*, 1998, **396**, 176–188.

21 H. Qin, P. Sutter and G. Zhou, *J. Am. Ceram. Soc.*, 2014, **97**, 2762–2769.

22 V. Rose and R. Franchy, *J. Appl. Phys.*, 2009, **105**, 07C902.

23 H. Graupner, L. Hammer, K. Heinz and D. M. Zehner, *Surf. Sci.*, 1997, **380**, 335–351.

24 Z. Dai, *PhD thesis*, Institut des NanoSciences de Paris, Paris, 2017.

25 R. M. Jaeger, H. Kuhlenbeck, H. J. Freund, M. Wuttig, W. Hoffmann, R. Franchy and H. Ibach, *Surf. Sci.*, 1991, **259**, 235–252.

26 A. Stierle, F. Renner, R. Streitel, H. Dosch, W. Drube and B. C. Cowie, *Science*, 2004, **303**, 1652–1656.

27 G. Kresse, M. Schmid, E. Napetschnig, M. Shishkin, L. Köhler and P. Varga, *Science*, 2005, **308**, 1440–1442.

28 S. Degen, A. Krupski, M. Kralj, A. Langner, C. Becker, M. Sokolowski and K. Wandelt, *Surf. Sci.*, 2005, **576**, L57–L64.

29 G. Hamm, C. Barth, C. Becker, K. Wandelt and C. R. Henry, *Phys. Rev. Lett.*, 2006, **97**, 126106.

30 M. Schmid, G. Kresse, A. Buchsbaum, E. Napetschnig, S. Gritschneder, M. Reichling and P. Varga, *Phys. Rev. Lett.*, 2007, **99**, 196104.

31 G. Kresse and J. Hafner, *Phys. Rev. B*, 1994, **49**, 14251–14269.

32 G. Kresse and J. Furthmüller, *Comp. Mater. Sci.*, 1996, **6**, 15–50.

33 G. Kresse and J. Furthmüller, *Phys. Rev. B*, 1996, **54**, 11169–11186.

34 G. Kresse and D. Joubert, *Phys. Rev. B*, 1999, **59**, 1758–1775.

35 P. Hohenberg and W. Kohn, *Phys. Rev.*, 1964, **136**, B864–B871.

36 W. Kohn and L. J. Sham, *Phys. Rev.*, 1965, **140**, A1133–A1138.

37 J. Klimeš, D. R. Bowler and A. Michaelides, *J. Phys.: Condens. Matter*, 2010, **22**, 022201.

38 J. Klimeš, D. R. Bowler and A. Michaelides, *Phys. Rev. B*, 2011, **83**, 195131.

39 H. J. Monkhorst and J. D. Pack, *Phys. Rev. B*, 1976, **13**, 5188–5192.

40 J. D. Pack and H. J. Monkhorst, *Phys. Rev. B*, 1977, **16**, 1748–1749.

41 M. Elstner, D. Porezag, G. Jungnickel, J. Elsner, M. Haugk, T. Frauenheim, S. Suhai and G. Seifert, *Phys. Rev. B*, 1998, **58**, 7260–7268.

42 M. Van den Bossche, H. Grönbeck and B. Hammer, *J. Chem.*

Theory Comput., 2018, **14**, 2797–2807.

43 The `Tango` and `Hotcent` codes are publicly available at https://gitlab.com/mvdb.

44 M. Van den Bossche, *J. Phys. Chem. A*, 2019, **123**, 3038–3045.

45 J. J. Mortensen, L. B. Hansen and K. W. Jacobsen, *Phys. Rev. B*, 2005, **71**, 035109.

46 J. Enkovaara, C. Rostgaard, J. J. Mortensen, J. Chen, M. Duak, L. Ferrighi, J. Gavnholt, C. Glinsvad, V. Haikola, H. A. Hansen, H. H. Kristoffersen, M. Kuisma, A. H. Larsen, L. Lehtovaara, M. Ljungberg, O. Lopez-Acevedo, P. G. Moses, J. Ojanen, T. Olsen, V. Petzold, N. A. Romero, J. Stausholm-Møller, M. Strange, G. A. Tritsaris, M. Vanin, M. Walter, B. Hammer, H. Häkkinen, G. K. H. Madsen, R. M. Nieminen, J. K. Nørskov, M. Puska, T. T. Rantala, J. Schiøtz, K. S. Thygesen and K. W. Jacobsen, *J. Phys.: Condens. Matter*, 2010, **22**, 253202.

47 M. A. L. Marques, M. J. T. Oliveira and T. Burnus, *Comput. Phys. Commun.*, 2012, **183**, 2272–2281.

48 B. Aradi, B. Hourahine and T. Frauenheim, *J. Phys. Chem. A*, 2007, **111**, 5678–5684.

49 A. R. Oganov, A. O. Lyakhov and M. Valle, *Acc. Chem. Res.*, 2011, **44**, 227–237.

50 S. M. Woodley and R. Catlow, *Nat. Mater.*, 2008, **7**, 937–946.

51 A. R. Oganov and C. W. Glass, *J. Phys.: Condens. Matter*, 2008, **20**, 064210.

52 L. B. Vilhelmsen and B. Hammer, *Phys. Rev. Lett.*, 2012, **108**, 126101.

53 L. B. Vilhelmsen and B. Hammer, *J. Chem. Phys.*, 2014, **141**, 044711.

54 S. R. Bahn and K. W. Jacobsen, *Comput. Sci. Eng.*, 2002, **4**, 56–66.

55 A. H. Larsen, J. J. Mortensen, J. Blomqvist, I. E. Castelli, R. Christensen, M. Duak, J. Friis, M. N. Groves, B. Hammer, C. Hargus, E. D. Hermes, P. C. Jennings, P. B. Jensen, J. Kermode, J. R. Kitchin, E. L. Kolsbjerg, J. Kubal, K. Kaasbjerg, S. Lysgaard, J. B. Maronsson, T. Maxson, T. Olsen, L. Pastewka, A. Peterson, C. Rostgaard, J. Schiøtz, O. Schütt, M. Strange, K. S. Thygesen, T. Vegge, L. Vilhelmsen, M. Walter, Z. Zeng and K. W. Jacobsen, *J. Phys. Condens. Matter*, 2017, **29**, 273002.

56 A. O. Lyakhov, A. R. Oganov, H. T. Stokes and Q. Zhu, *Comput. Phys. Commun.*, 2013, **184**, 1172–1182.

57 E. Menéndez-Proupin and G. Gutiérrez, *Phys. Rev. B*, 2005, **72**, 035116.

58 H. P. Pinto, R. M. Nieminen and S. D. Elliott, *Phys. Rev. B*, 2004, **70**, 125402.

59 Y. Repelin and E. Husson, *Mat. Res. Bull.*, 1990, **25**, 611–621.

60 G. Paglia, C. E. Buckley, A. L. Rohl, B. A. Hunter, R. D. Hart, J. V. Hanna and L. T. Byrne, *Phys. Rev. B*, 2003, **68**, 144110.

61 G. Paglia, A. L. Rohl, C. E. Buckley and J. D. Gale, *Phys. Rev. B*, 2005, **71**, 224115.

62 X. Krokidis, P. Raybaud, A.-E. Gobichon, B. Rebours, P. Euzen and H. Toulhoat, *J. Phys. Chem. B*, 2001, **105**, 5121–5130.

63 L. Kovarik, M. Bowden, A. Genc, J. Szanyi, C. H. F. Peden and J. H. Kwak, *J. Phys. Chem. C*, 2014, **118**, 18051–18058.

64 T. Yokokawa and O. J. Kleppa, *J. Phys. Chem.*, 1964, **68**, 3246–3249.

65 M. F. Peintinger, M. J. Kratz and T. Bredow, *J. Mater. Chem. A*, 2014, **2**, 13143–13158.

66 K. Momma and F. Izumi, *J. Appl. Crystallogr.*, 2011, **44**, 1272–1276.

67 J. Frenzel, A. F. Oliveira, H. A. Duarte, T. Heine and G. Seifert, *Z. Anorg. Allg. Chem.*, 2005, **631**, 1267–1271.

68 R. Caracas and R. E. Cohen, *Geophys. Res. Lett.*, 2005, **32**, 1–4.

69 A. R. Oganov and S. Ono, *PNAS*, 2005, **102**, 10828–10831.

70 S. Blonski and S. H. Garofalini, *Surf. Sci.*, 1993, **295**, 263–274.

71 I. Manassidis and M. J. Gillan, *J. Am. Ceram. Soc.*, 1994, **77**, 335–338.

72 N. H. de Leeuw and S. C. Parker, *J. Am. Ceram. Soc.*, 1999, **82**, 3209–2316.

73 A. P. Borosy, B. Silvi, M. Allavena and P. Nortier, *J. Phys. Chem.*, 1994, **98**, 13189–13194.

74 Z. Łodziana, N.-Y. Topsøe and J. K. Nørskov, *Nat. Mater.*, 2004, **3**, 289–293.

75 M. Digne, P. Sautet, P. Raybaud, P. Euzen and H. Toulhoat, *J. Catal.*, 2004, **226**, 54–68.

76 A. Walsh and C. R. A. Catlow, *J. Mater. Chem.*, 2010, **20**, 10438–10444.

77 J. Goniakowski, S. Bouette-Russo and C. Noguera, *Surf. Sci.*, 1993, **284**, 315–327.

78 M.-C. Desjonqueres and D. Spanjaard, *Concepts in Surface Physics*, Springer-Verlag, Berlin Heidelberg, 1993.

79 L. Pauling, *J. Am. Chem. Soc.*, 1929, **51**, 1010–1026.

80 I. D. Brown and R. D. Shannon, *Acta Cryst. A*, 1973, **29**, 266–282.

81 J. H. Dycus, K. J. Mirrielees, E. D. Grimley, R. Kirste, S. Mita, Z. Sitar, R. Collazo, D. L. Irving and J. M. LeBeau, *ACS Appl. Mater. Interfaces*, 2018, **10**, 10607–10611.

82 T. J. Godin and J. P. LaFemina, *Phys. Rev. B*, 1994, **49**, 7691–7696.

83 A. J. Rowley, M. Wilson and P. A. Madden, *J. Phys.: Condens. Matter*, 1999, **11**, 1903–1914.

84 R. Baxter, P. Reinhardt, N. López and F. Illas, *Surf. Sci.*, 2000, **445**, 448–460.

85 J. Goniakowski, F. Finocchi and C. Noguera, *Rep. Prog. Phys.*, 2007, **71**, 016501.

86 J. Goniakowski, C. Noguera and L. Giordano, *Phys. Rev. Lett.*, 2007, **98**, 205701.

87 A. Navrotsky, *Geochem. Trans.*, 2003, **4**, 34–37.

88 J. Goniakowski, C. Noguera and L. Giordano, *Phys. Rev. Lett.*, 2004, **93**, 215702.

89 Y. Xin, P. D. Brown, C. J. Humphreys, T. S. Cheng and C. T. Foxon, *Appl. Phys. Lett.*, 1997, **70**, 1308–1310.

90 Z. Y. Al Balushi, K. Wang, R. K. Ghosh, R. A. Vilá, S. M. Eichfeld, J. D. Caldwell, X. Qin, Y.-C. Lin, P. A. DeSario, G. Stone, S. Subramanian, D. F. Paul, R. M. Wallace, S. Datta, J. M. Redwing and J. A. Robinson, *Nat. Mater.*, 2016, **15**, 1166–1171.

91 S. Mohn, N. Stolyarchuk, T. Markurt, R. Kirste, M. P. Hoff-

mann, R. Collazo, A. Courville, R. Di Felice, Z. Sitar, P. Ven-néguès and M. Albrecht, *Phys. Rev. Appl.*, 2016, **5**, 054004.

92 A. Rečnik, N. Daneu, T. Walther and W. Mader, *J. Am. Ceram. Soc.*, 2001, **84**, 2657–2668.

93 M. B. Ullah, V. Avrutin, S. Q. Li, S. Das, M. Monavarian, M. Toporkov, U. Özgür, P. Ruterana and H. Morkoç, *Phys. Status Solidi RRL*, 2016, **10**, 682–686.

94 K. Nomura, H. Ohta, K. Ueda, T. Kamiya, M. Hirano and H. Hosono, *Science*, 2003, **300**, 1269–1272.